Lyapunov-Induced Model Predictive Power Control for Grid-Tie Three-Level Neutral-Point-Clamped Inverter With Dead-Time Compensation

Van-Quang-Binh Ngo, Van-Hiep Vu, Viet-Tuan Pham, Huu-Nhan Nguyen, Pedro Rodriguez-Ayerbe, Sorin Olaru, Hoang-Thinh Do

Date of publication xxxx 00, 0000, date of current version xxxx 00, 0000.

Lyapunov-Induced Model Predictive Power Control for Grid-tie Three-level Neutral-Point-Clamped Inverter with Dead-time Compensation

VAN-QUANG-BINH NGO[1,2], VAN-HIEP VU[3], VIET-TUAN PHAM[2], HUU-NHAN NGUYEN[1], PEDRO RODRIGUEZ-AYERBE[4], SORIN OLARU[4] and HOANG-THINH DO[5]

[1]Institute of Research and Development, Duy Tan University, Da Nang 550000, Vietnam (e-mail: qbinhtam@gmail.com; huunhan.vn@gmail.com).
[2]Faculty of Physics, University of Education, Hue University, Thua Thien Hue 530000, Vietnam (e-mail: phamviettuan@gmail.com).
[3]NTT Hi-Tech Institute, Nguyen Tat Thanh University, Ho Chi Minh City 70000, VietNam (e-mail: vvhiep@ntt.edu.vn).
[4]Laboratory of Signals and Systems (L2S), CentraleSupélec-CNRS-University Paris-Sud-Paris Saclay University, Gif sur Yvette 91192, France (e-mail: Pedro.Rodriguez@centralesupelec.fr; Sorin.Olaru@centralesupelec.fr).
[5]Division of Computational Mechatronics, Institute for Computational Science, Ton Duc Thang University, Ho Chi Minh City, Vietnam; Faculty of Electrical & Electronics Engineering, Ton Duc Thang University, Ho Chi Minh City, Vietnam.

Corresponding author: Hoang-Thinh Do (e-mail: dohoangthinh@tdtu.edu.vn).

ABSTRACT In this paper, a new power control strategy based on a model predictive power control for the grid-tie three-level neutral point clamped inverter is presented. A dynamical model based on the orientation of grid voltage is used to predict the performance of control variables required for the system. A cost function that includes the tracking power ability, the neutral-point voltage balancing and switching frequency reduction is used to achieve the optimal switching state. A proposed selection scheme of control input is introduced to comprehend the stability of the closed-loop system and reduce the computational cost. At each sampling time, only candidate switching state inputs that guarantee the stability condition through a control Lyapunov function is evaluated in the cost function of the MPC algorithm. Thus, the execution time is remarkably decreased by 26% in comparison with traditional model predictive control. Moreover, the dead-time effect is compensated by incorporating its influence in the proposed prediction model. Simulation and experimental results compared with the traditional model predictive control are used to confirm the effectiveness of the proposed scheme.

INDEX TERMS Computational burden, Control Lyapunov function, Dead-time compensation, Finite control set model predictive control, Stability conditions, Three-level Neutral-Point-Clamped inverter.

NOMENCLATURE

C_1, C_2, C_{dc}	DC-link capacitance.
i_g, u_g	Grid current and voltage.
i_z	Neutral-point current.
K_d, K_q	Positive gains of Lyapunov function.
L_f, R_f	Filter inductance and resistance.
ω	Grid voltage angular frequency.
θ	Grid voltage angle in the stationary frame.
λ_{uz}, λ_{sw}	Weighting factor of voltage balance, switching frequency reduction.
P_g, Q_g	Grid active and reactive powers.
S_x	Switching state of the 3L-NPC inverter.
t_d, t_{on}, t_{off}	Dead-time, turn-on/off time of IGBT.
T_s	Sampling time of the controller.
u_{inv}	Inverter output voltage.
U_{dc}	DC-bus voltage.
u_z	Neutral-point voltage.
Superscripts	
$*$	Reference value.
p	Predicted value.
Subscripts	
d, q	d, q axis of grid voltage oriented reference frame.
α, β	α, β axis of stationary reference frame.

I. INTRODUCTION

Multilevel inverters have been extensively applied to high power electronics due to their benefits in the increment of the

capacity and in the improvement of the performance. Among them, three-level neutral point-clamped (3L-NPC) inverters become particularly attractive as an alternative solution thanks to their advantageous features such as low total harmonic distortion (THD) of the output current and common-mode voltage [1], [2]. Moreover, the 3L-NPC inverters have some advantages compared with the conventional two-level inverters, for example, the half voltage stress on the power switching devices and lower dv/dt in the output voltage. The main issue of the 3L-NPC inverter is the unbalance of the DC-link capacitor voltage can be addressed based on several control strategies [1], [3]–[5].

Recently, the inverters have been widely used to connect the electrical grid. Grid-tie inverters have an important role in applications such as flexible alternating current transmission systems, and renewable energy systems [6], especially the photovoltaic power system [7]. For this reason, stable and adequate control is necessary for grid-connected inverters. In the past, many control methods have been proposed for grid-tie 3L-NPCs. The most popular one is based on the orientation of the grid voltage [8] with two control loops to regulate the grid active and reactive power flow. The component of the grid current and DC voltage are regulated by the inner and outer control loops, respectively. This method allows to control the current components and the active/reactive powers independently of each other. However, the transient response is relatively slow. The high-performance control requires precise parameters for the PI current controllers.

In recent years, direct power control (DPC) scheme [9] has been introduced to enhance the performance of grid-tie systems. This approach employs a look-up table (LUT) and the angle of the grid voltage or virtual flux to obtain suitable switching states. Hence, this leads to a simple structure due to no necessity of the current control loop and pulse width modulation. Nonetheless, the large power ripples and switching frequency variation are the disadvantages of LUT. Furthermore, to ensure a satisfactory control performance of LUT-DPC, a high sampling frequency is required. In addition, both linear and hysteresis techniques are unable to incorporate the constraints and special necessities such as maximum current, THD of the load current, and switching frequency. To overcome these problems several techniques have been proposed such as proportional resonant [10], DPC based on fuzzy logic and pulse width modulation [11], sliding mode control [12], predictive current control [13]–[17], and predictive power control [18]. In order to reduce the distortion of the output current, neutral-point voltage, and neutral-point current [19], [20], it is necessary to consider the dead-time effect in the control design.

Nowadays, finite control set model predictive control (FCS-MPC) is recognized as a comprehensive control method for power converters thanks to its potential benefits such as simple concept and straightforward incorporation of nonlinearities, additional static constraint, and management of the computational time delay [21]–[27]. In addition, the predictive control achieves a fast dynamic response and an implementation simplicity. Nevertheless, in the FCS-MPC, the optimal control input is obtained from the evaluation of the cost function for all switching states and results in an increased calculation time, particularly with a large amount of switching state and long prediction horizons. To solve this issue, a simplified FCS-MPC for grid connected power converter is proposed in [28] which decreases the computational time by using the equivalent transformation in the cost function and sector distribution of voltage vector. Another method is proposed in [29] which employs the best switching sequence MPC to provide fixed switching frequency and maintain restricted computational cost. In [30], [31], the authors presented a practical stability theory to obtain a useful cost function by determining the terminal weighting matrix concerning the linear quadratic regulator solution. Previous work has been limited to the nonlinear system due to the balance of DC-link capacitor voltages of the 3L-NPC inverter. A Lyapunov function derived from the predictive model [32], [33] is introduced for the three-phase two-level voltage source converter to address the stability issue. Their solutions are based on the voltage reference vector in the cost function to reduce the computational time. However, this technique not well suited to a multilevel inverter due to the integration of dead-time in the evaluation of the optimization problem with all switching control inputs. Another approach is presented in [5] uses sector distribution and feasible candidate inverter voltage to reduce the execution time and maintain the balanced voltage for DC-bus capacitors. Nevertheless, this method is just employed in 3L-T-type inverter with RL load.

Although several studies have been devoted to computational burden, less attention has been paid to consider the stability of the FCS-MPC method. In this paper, the development of a direct power control strategy based on a prediction model for grid-tie 3L-NPC inverter is presented. The proposed method controls the grid power flow, keeps the neutral-point voltage balancing and reduces the switching frequency. The main contribution of this paper aims to consider the closed-loop stability of the system in the control design. In order to ensure the stability of the system, only candidate switching inputs that guarantee the stability condition derived from a Lyapunov function are taken into account in the evaluation of the cost function. Therefore, the computational burden of the proposed method is reduced by 26% compared to that of the conventional FCS-MPC, resulting in the possibility of real-time implementation. Furthermore, this study focuses on the system modeling which includes the dead-time and switching-time delays caused by the commutated transition of the power converters. In this case, the output and neutral-point voltages can be compensated by using the proposed predictive dynamic model, leading to the improvement of system performance.

The remainder of the paper is structured as follows: Section II presents the dynamic model of a grid-connected 3L-NPC inverter with taking into account the dead-time effect. Next, section III details the proposed Lyapunov function-based model predictive control for the system. In section IV,

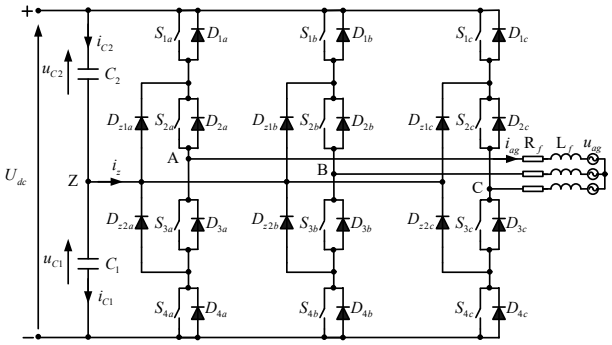

FIGURE 1: Configuration of the grid-tie 3L-NPC inverter.

a comparative investigation between the proposed method and conventional FCS-MPC is performed in simulation and experimental results. Lastly, the conclusions are outlined in Section V.

II. PREDICTIVE POWER MODEL OF 3L-NPC GRID-TIE INVERTER

A. STRUCTURE

Fig. 1 shows a simplified diagram of the grid-tie 3L-NPC inverter. Three possible switching states "1", "0" and "-1" are used to indicate the operating principle of the 3L-NPC inverter. The switching state "1" or "P" denotes two switches S_{1a} and S_{2a} in branch A are turned "ON" and the inverter output voltage u_{AZ} is equal to $U_{dc}/2$, while two switches S_{1a} and S_{2a} are switched "OFF" with "-1" or "N", leading to $u_{AZ} = -U_{dc}/2$. The switching state "0" or "O" signifies two internal switches S_{2a} and S_{3a} are turned "ON". According to the direction of the grid current, the output voltage is fixed to zero throughout the NPC diodes D_{z1a} or D_{z2a}. Thus, there are a total of 27 possible configurations with the 3L-NPC inverter. Table 1 summarizes the conduction states produced by the 3L-NPC inverter.

TABLE 1: Conduction state of the inverter leg with $x \in \{a, b, c\}$

S_x	Status of switches				Inverter voltage	Neutral-point
	S_{1x}	S_{2x}	S_{3x}	S_{4x}	u_{AZ}	current i_{zx}
1	ON	ON	OFF	OFF	$U_{dc}/2$	0
0	OFF	ON	ON	OFF	0	i_{xg}
-1	OFF	OFF	ON	ON	$-U_{dc}/2$	0

B. MATHEMATICAL MODEL

The output voltage created by the 3L-NPC inverter is formulated in term of phase voltage as:

$$u_{inv} = \frac{2}{3}\left(u_{AZ} + k u_{BZ} + k^2 u_{CZ}\right), \tag{1}$$

with $k = e^{j2\pi/3} = -\frac{1}{2} + j\frac{\sqrt{3}}{2}$.

The phase voltage u_{xZ} is computed based on the DC-bus voltage (U_{dc}) and conduction state (S_x) as follows [13], [21]:

$$u_{xZ} = S_x \frac{U_{dc}}{2}, \tag{2}$$

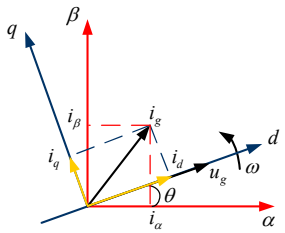

FIGURE 2: Reference system frames.

where S_x indicates the status of the inverter branch: $S_x \in \{-1, 0, 1\}$ with $x \in \{a, b, c\}$.

The dynamic model of grid side inverter can be described by:

$$u_{inv} = u_g + R_f i_g + L_f \frac{di_g}{dt}, \tag{3}$$

where $i_g = [i_{ag}\ i_{bg}\ i_{cg}]^T$, $u_g = [u_{ag}\ u_{bg}\ u_{cg}]^T$ represent the grid current and voltage. L_f, R_f signify the filter inductance and resistance, respectively.

By employing the Clarke transformation, the inverter output voltage is given as:

$$u_{inv} = \frac{U_{dc}}{6}\Big(2S_a - S_b - S_c + j\sqrt{3}\big(S_b - S_c\big)\Big). \tag{4}$$

The model of the grid side inverter in the dq frame is taken from the Park transformation of (3) as:

$$\begin{aligned} u_{inv\_d} &= R_f i_d + L_f \frac{di_d}{dt} + u_d - \omega L_f i_q, \\ u_{inv\_q} &= R_f i_q + L_f \frac{di_q}{dt} + u_q + \omega L_f i_d, \end{aligned} \tag{5}$$

where $\omega = 2\pi f_g$ is the grid frequency.

The grid voltage component can be obtained with the assumption of the grid-voltage orientation as shown in Fig. 2:

$$u_d = \hat{U}_m,\ u_q = 0, \tag{6}$$

where $\hat{U}_m$ expresses the estimated grid voltage amplitude derived from the phase-locked loop (PLL).

Assuming constant DC-link voltage, the dynamic behavior of neutral-point voltage (Z) is achieved from the grid currents and the conduction states as [5]:

$$\begin{aligned} \frac{du_z}{dt} &= \frac{d(u_{C1} - u_{C2})}{dt} = -\frac{1}{C_{dc}} i_z \\ &= \frac{1}{2C_{dc}}\Big(2\,|S_a| - |S_b| - |S_c|\Big) i_\alpha + \frac{\sqrt{3}}{2C_{dc}}\Big(|S_b| - |S_c|\Big) i_\beta, \end{aligned} \tag{7}$$

where $C_1 = C_2 = C_{dc}$ is the DC-link capacitance.

Therefore, the continuous-time model of the system dynamics in the dq synchronous frame can be expressed based on (5), (6), and (7):

$$\begin{aligned}\frac{di_d}{dt} &= -\frac{R_f}{L_f}i_d + \frac{1}{L_f}(u_{inv\_d} - \hat{U}_m) + \omega i_q, \\ \frac{di_q}{dt} &= -\frac{R_f}{L_f}i_q + \frac{1}{L_f}u_{inv\_q} - \omega i_d, \\ \frac{du_z}{dt} &= \frac{1}{2C_{dc}}\big(2|S_a| - |S_b| - |S_c|\big)i_\alpha \\ &\quad + \frac{\sqrt{3}}{2C_{dc}}\big(|S_b|) - |S_c|\big)i_\beta,\end{aligned} \tag{8}$$

where the grid current component in the synchronous dq frame is derived from its value in the stationary reference $\alpha\beta$ via the rotational coordinate transformation:

$$\begin{aligned} i_d &= i_\alpha \cos\theta + i_\beta \sin\theta, \\ i_q &= i_\beta \cos\theta - i_\alpha \sin\theta. \end{aligned} \tag{9}$$

The inverter output voltage in the synchronous frame is given in the same way based on (1) and (3) as:

$$\begin{aligned} u_{inv\_d} &= \frac{U_{dc}}{6}\Big(\big(2S_a - S_b - S_c\big)\cos\theta + \sqrt{3}\big(S_b - S_c\big)\sin\theta\Big), \\ u_{inv\_q} &= \frac{U_{dc}}{6}\Big(\sqrt{3}\big(S_b - S_c\big)\cos\theta - \big(2S_a - S_b - S_c\big)\sin\theta\Big). \end{aligned} \tag{10}$$

The grid active and reactive powers are computed as follows [9]:

$$\begin{aligned} P_g &= \frac{3}{2}\left(u_d i_d + u_q i_q\right) = \frac{3}{2}\hat{U}_m i_d, \\ Q_g &= \frac{3}{2}\left(u_q i_g - u_d i_q\right) = -\frac{3}{2}\hat{U}_m i_q. \end{aligned} \tag{11}$$

Equation (11) indicates that we can decouple the grid active and reactive power flow via the components of the current in dq axis.

C. AVERAGE VOLTAGE AND CURRENT COMPENSATIONS OF PREDICTION MODEL

The dead-time is required to avoid the simultaneous transition of two switches of each inverter branch in the real system. The effect of the dead-time is to increase the distortion and the ripple of the inverter voltage and grid current leading to an increment of the THD [19], [20]. In [34], the dead-time impact is considered in the prediction model but only incorporating the dead-time delay. In order to decrease the dead-time effects, our study proposes a new average voltage compensation to improve control performance. The inverter voltage during the commutation of switching transition is established based on the previous and existing switching states and the flow of the grid current. Fig. 4(a) shows the commutated transition from the switching state "0" to "1". Switches S_{2a} and S_{3a} are turned "ON" at state "0". The NPC diode D_{z1a} is switched "ON" with the positive grid current ($i_{ag} > 0$). In the ideal case, two switches S_{1a} and S_{3a} are turn "ON" and "OFF" simultaneously. Thus, the inverter output voltage steps from zero to $U_{dc}/2$. When considering the dead-time and turn-on delays, the real switching signals and the output voltage can be approximated as demonstrated in Fig. 3(a). After the dead-time period, S_{1a} changes from "OFF" to "ON" with the remaining load current i_{ag}. However, it takes the turn-on time to be completely commutated. Then, the load current is switched from D_{z1a} to S_{1a} and the output voltage is stepped to $U_{dc}/2$ after the dead-time and turn-on delays as shown in Fig. 4(a). This means that the actual output voltage is reduced by $t_d + t_{on}$ and illustrated as the rectangular pattern in Fig. 3(a). On the other hand, in a "1" to "0" transition, S_{1a} is switched "OFF" and S_{3a} is commutated "ON" after the dead-time. S_{1a} is continuously conducted due to the turn-off time t_{off}, resulting in the remain of the output voltage ($U_{dc}/2$). Therefore, the output voltage is changed to zero after the turn-off delay. In such case, the conduction state "1" is stretch out by t_{off}. In summary, the impact of dead-time and switching time delays on the output voltage for each transition is shown in Figs. 3 and 4. Consequently, the actual inverter voltage $u_{xZ\text{-}real}$ generated during a sampling period T_s can be given based on Table 2 as:

$$u_{xZ-real}(k) = \begin{cases} \dfrac{T_s - t_d - t_{on}}{T_s}u_{xZ}(k), & \textbf{5} \text{ is assured}, \\ \dfrac{t_{off}}{T_s}u_{xZ}(k-1), & \textbf{6} \text{ is assured}, \\ \dfrac{T_s - t_{off}}{T_s}u_{xZ}(k), & \textbf{7} \text{ is assured}, \\ \dfrac{t_d + t_{on}}{T_s}u_{xZ}(k-1), & \textbf{8} \text{ is assured}, \\ u_{xZ}(k) & \text{otherwise}. \end{cases} \tag{12}$$

TABLE 2: Commutation conditions of the inverter based on the switching state and the flow of the current

Case	Condition state
1	$(S_x(k-1)=0)\,\&\,(S_x(k)=1)$
2	$(S_x(k-1)=-1)\,\&\,(S_x(k)=0)$
3	$(S_x(k-1)=1)\,\&\,(S_x(k)=0)$
4	$(S_x(k-1)=0)\,\&\,(S_x(k)=-1)$
5	$((sign(i_{xg})>0)\,\&\textbf{1}) \vee ((sign(i_{xg})<0)\,\&\textbf{4})$
6	$((sign(i_{xg})>0)\,\&\textbf{3}) \vee ((sign(i_{xg})<0)\,\&\textbf{2})$
7	$((sign(i_{xg})<0)\,\&\textbf{1}) \vee ((sign(i_{xg})>0)\,\&\textbf{4})$
8	$((sign(i_{xg})<0)\,\&\textbf{3}) \vee ((sign(i_{xg})>0)\,\&\textbf{2})$

Moreover, the neutral-point voltage is also influenced by the dead-time due to the neutral-point currents as shown in Fig. 4 [35]. With the aim to explicate this impact, the transition state from "-1" to "0" with $i_{ag} < 0$ is considered as an illustration (Fig. 4(d)). In "-1" state, S_{3a} and S_{4a} are switched "ON" and the current is conducted by S_{3a} and S_{4a}. As S_{3a} is in the state "ON" during the dead-time and state "0" periods, the neutral-point current ($i_{za} = i_{ag}$) is transmitted by S_{3a} and D_{z2a}. The commutation is transferred after S_{4a} is fully turned "OFF" with turn-off time t_{off}. Hence, the neutral-point current i_{za} is conducted within $T_s - t_{off}$

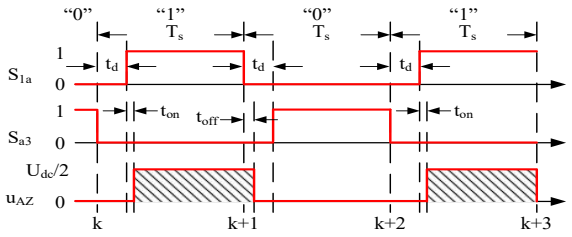

(a) Dead-time effect of switching states "0" and "1" with $i_{ag} > 0$

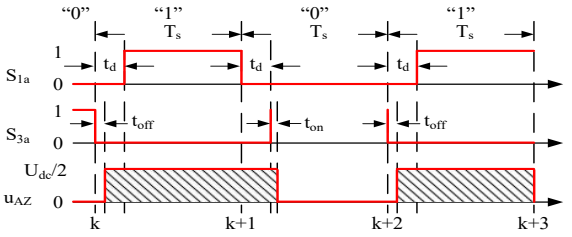

(b) Dead-time effect of switching states "0" and "1" with $i_{ag} < 0$

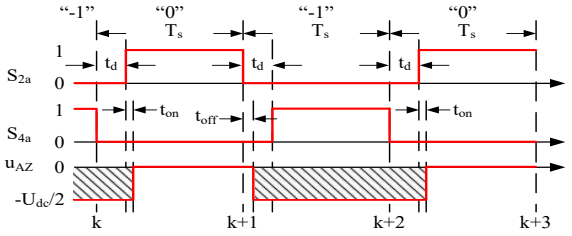

(c) Dead-time effect of switching states "-1" and "0" with $i_{ag} > 0$

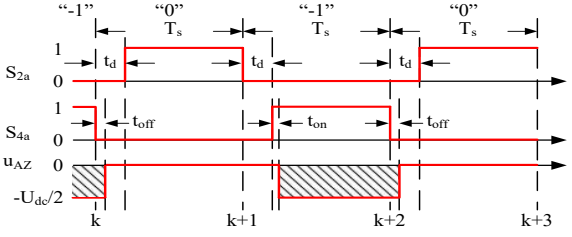

(d) Dead-time effect of switching states "-1" and "0" with $i_{ag} < 0$

FIGURE 3: The impact of dead-time and switching time delays on output voltage.

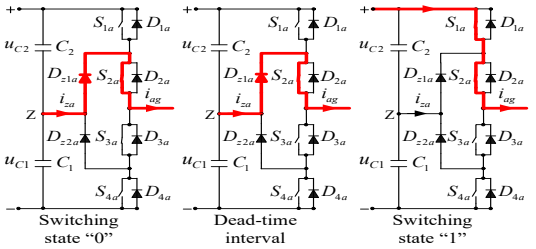

(a) Commutation from switching state "0" to "1" with $i_{ag} > 0$

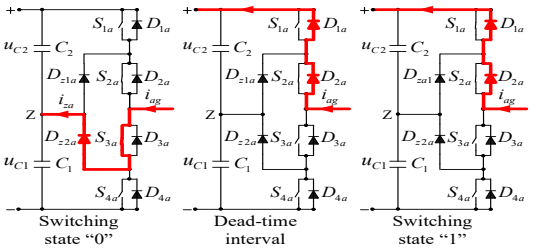

(b) Commutation from switching state "0" to "1" with $i_{ag} < 0$

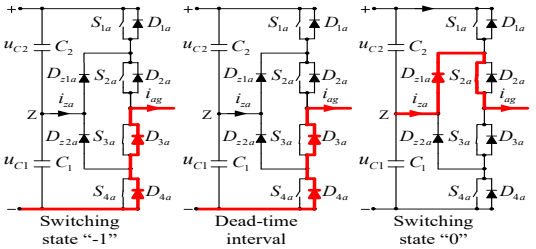

(c) Commutation from switching state "-1" to "0" with $i_{ag} > 0$

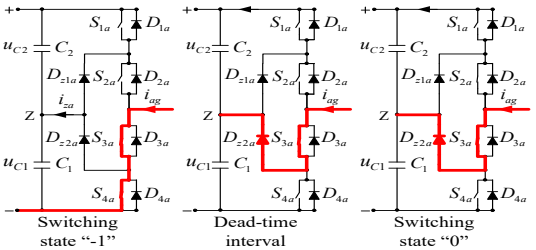

(d) Commutation from switching state "-1" to "0" with $i_{ag} < 0$

FIGURE 4: Commutation process during the dead-time.

time. Therefore, the neutral-point current of one phase which incorporates the dead-time effect can be expressed as:

$$i_{zx} = \begin{cases} \dfrac{t_d + t_{on}}{T_s} i_{xg}, & \text{if case } \mathbf{5} \text{ is assured,} \\ \dfrac{T_s - t_{off}}{T_s} i_{xg}, & \text{if case } \mathbf{6} \text{ is assured,} \\ \dfrac{t_{off}}{T_s} i_{xg}, & \text{if case } \mathbf{7} \text{ is assured,} \\ \dfrac{T_s - t_d - t_{on}}{T_s} i_{xg}, & \text{if case } \mathbf{8} \text{ is assured,} \\ (1 - |S_x|) i_{xg}, & \text{otherwise,} \end{cases} \tag{13}$$

where i_{zx} represents the neutral-point current of one phase.

The dynamic behavior of neutral-point voltage which compensates the dead-time effect is rewritten based on (7):

$$\frac{du_{z-real}}{dt} = -\frac{1}{C_{dc}} i_{z-real} = -\frac{1}{C_{dc}} \left(i_{za} + i_{zb} + i_{zc} \right), \tag{14}$$

with i_{za}, i_{zb}, i_{zc} given by (13).

As a result, we can compensate for the dead-time effect by considering its impact with the modified predictive voltage and current in (12), (13), and (14).

III. PROPOSED LYAPUNOV MODEL PREDICTIVE POWER CONTROL

The proposed predictive control strategy aims to:

- Pursue grid active and reactive power references.
- Conserve the capacitor voltage balancing of DC-bus.

- Diminish the switching frequency.

With the purpose of fulfilling these control goals, the cost function of the grid-tie 3L-NPC inverter with a computational time delay can be expressed [21], [36]:

$$g(u_{k+1}) = \left|P_g^*(k+2) - P_g^p(k+2)\right| + \lambda_{uz}\left|u_z^p(k+2)\right| + \left|Q_g^*(k+2) - Q_g^p(k+2)\right| + \lambda_{sw} n_{sw}, \quad (15)$$

where $P_g^*(k+2)$, $Q_g^*(k+2)$ and $P_g^p(k+2)$, $Q_g^p(k+2)$ stand for the future reference and predicted values of the active and reactive powers at instant $k+2$. λ_{uz}, λ_{sw} indicate the weighting elements of the voltage balancing of DC-bus and reduced switching frequency, respectively.

n_{sw} is considered as the auxiliary constraint of the cost function to limit the range of switching frequency. Hence, it can be formulated as:

$$n_{sw} = \sum_{x=a,b,c} |S_x(k+1) - S_x(k)|. \quad (16)$$

The discrete-time evaluation of the grid current during a sampling time T_s is achieved utilizing the first-order forward Euler's method for (8):

$$\hat{i}_d(k+1) = i_d(k)\left(1 - \frac{T_s R_f}{L_f}\right) + \frac{T_s}{L_f}\left(u_{inv\_d}(k) - \hat{U}_m\right) + T_s\omega i_q(k), \quad (17)$$

$$\hat{i}_q(k+1) = i_q(k)\left(1 - \frac{T_s R_f}{L_f}\right) + \frac{T_s}{L_f}u_{inv\_q}(k) - T_s\omega i_d(k),$$

where $u_{inv\_d}(k), u_{inv\_q}(k)$ denote the real output voltage considering dead-time compensation are calculated by using (12) and Park transformation.

Similarly, the expression of discrete-time for grid current at sampling instant $k+2$ is given by:

$$i_d^p(k+2) = \hat{i}_d(k+1)\left(1 - \frac{T_s R_f}{L_f}\right) + \frac{T_s}{L_f}u_{inv\_d}(k+1) - \frac{T_s}{L_f}\hat{U}_m + T_s\omega\hat{i}_q(k+1), \quad (18)$$

$$i_q^p(k+2) = \hat{i}_q(k+1)\left(1 - \frac{T_s R_f}{L_f}\right) + \frac{T_s}{L_f}u_{inv\_q}(k+1) - T_s\omega\hat{i}_d(k+1),$$

The dynamic behavior of neutral-point voltage is achieved using (14). Then its expression is given by:

$$\hat{u}_z(k+1) = u_z(k) - \frac{T_s}{C_{dc}}\left(i_{za}(k) + i_{zb}(k) + i_{zc}(k)\right),$$

$$u_z^p(k+2) = u_z^p(k+1) - \frac{T_s}{C_{dc}}\left(i_{za}^p(k+1) + i_{zb}^p(k+1)\right) - \frac{T_s}{C_{dc}}i_{zc}^p(k+1), \quad (19)$$

where $i_{dc1x}(k)$ and $i_{dc1x}^p(k+1)$ are the neutral-point currents estimated based on (13).

In order to reduce the computational cost, the predictive future references can be achieved by simple extrapolation as:

$$P_g^*(k+2) = P_g^*(k+1) = P_g^*(k), \quad (20)$$
$$Q_g^*(k+2) = Q_g^*(k+1) = Q_g^*(k).$$

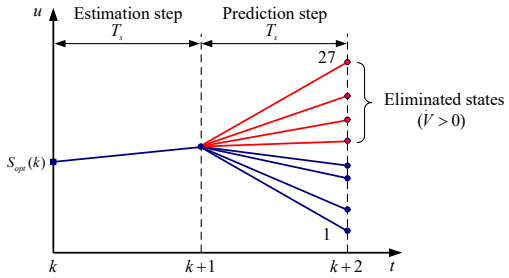

FIGURE 5: The modified control algorithm with decreased candidate input.

The errors of the grid current $\tilde{i}_{gd}$, $\tilde{i}_{qq}$ are described:

$$\tilde{i}_d = i_d - i_d^*, \quad (21)$$
$$\tilde{i}_q = i_q - i_q^*,$$

where the grid current references are calculated based on (11)

$$i_d^* = \frac{2P_g^*}{3\hat{U}_m}, \quad (22)$$
$$i_q^* = -\frac{2Q_g^*}{3\hat{U}_m}.$$

Replacing into the dynamic model given by (8), we have the error dynamic system of the grid current as:

$$\frac{d\tilde{i}_d}{dt} = -\frac{R_f}{L_f}i_d + \frac{1}{L_f}u_{inv\_d} + \omega i_q - \frac{di_d^*}{dt}, \quad (23)$$
$$\frac{d\tilde{i}_q}{dt} = -\frac{R_f}{L_f}i_q + \frac{1}{L_f}u_{inv\_q} - \frac{1}{L_f}\hat{U}_m - \omega i_d - \frac{di_q^*}{dt}.$$

Since the sampling frequency of the controller (f_s = 20 kHz) is greater than grid frequency (f_g = 50 Hz), we can assume that:

$$\frac{di_d^*}{dt} = 0; \ \frac{di_q^*}{dt} = 0. \quad (24)$$

As reported by (11), the grid current can be used to regulate the power flow. In our study, a control Lyapunov function is employed in the proposed method to guarantee the ability of tracking of their powers P_g^*, Q_g^*:

$$V\left(\tilde{i}_d, \tilde{i}_q\right) = \frac{1}{2}K_d\tilde{i}_d^2 + \frac{1}{2}K_q\tilde{i}_q^2, \quad (25)$$

with derivative

$$\dot{V}\left(\tilde{i}_d, \tilde{i}_q\right) = K_d\tilde{i}_d\frac{d\tilde{i}_d}{dt} + K_q\tilde{i}_q\frac{d\tilde{i}_q}{dt}, \quad (26)$$

where K_d and K_q are the positive gains.

The control input is a combination of switching state $S_p = [S_{pa}\ S_{pb}\ S_{pc}]^T$ with $x \in \{a,b,c\}$, whereas p belongs to a finite set $\{1,...,27\}$. Furthermore, each control input S_{px} is bounded to a set $\{-1,0,1\}$. Consequently, the control input S_{opt} is obtained as the result of (27):

$$S_{opt} = \arg\left\{\min_{u_{k+1}\in\{-1,0,1\}^3} g\left(u_{k+1}\right)\right\}. \quad (27)$$

In a real-time system, a computational time delay is inevitable. To deal with this issue, the classical FCS-MPC [21], [36] employs the approximated values to compensate for the computational requirement. Then, a control input which is obtained by minimizing the cost function at the prediction step $k+2$ is implemented to the inverter at the previous instant. As was noted in section II-A, there are 27 switching state inputs of the 3L-NPC inverter. With the traditional FCS-MPC, we have to calculate 27 predictions of the grid current, neutral-point voltage balancing, and grid powers. Moreover, it also requires the measured time of the control variables such as voltage, current to accomplish the control input. Subsequently, a large computational burden is the significant drawback of the conventional FCS-MPC, causing difficulty in the practical implementation of the algorithm at a high sampling rate. To decrease the computational time, we employ a pruning technique based on the decreasing Lyapunov function as shown in Fig. 5. At each sampling time, only switching candidates which have a negative $\dot{V}$ are evaluated in the cost function of the MPC algorithm. Figs. 6(a) and 6(b) illustrate the Lyapunov function and its derivative. These figures indicate that the stability of the closed-loop system is ensured when the $\dot{V}$ is negative at each moment. As suggested in [37], at least one switching state will ensure the stability at each prediction interval. For constant reference currents at least one of the switches will produce current evolution (23) in order to assure a decreasing of the Lyapunov function (25). In addition, not all switches will produce a decreasing in the Lyapunov function, as the symmetric of the switches producing a decreasing of the Lyapunov will produce an increase on this function. Fig. 6(c) shows the effect of each switching state which satisfies the stability condition ($\dot{V} < 0$) are considered for the minimization loop. Several unstable switching states can be eliminated for prediction and assessment of the cost function as detailed in Fig. 6(c). Therefore, this paper underlines the reduction of computational burden by incorporating the stability condition. With the purpose of illustrate this process, Fig. 6(d) details the selection of 10 switching states. For instance at time $t = 0.1632$ s, three switching states (state 2, 3, and 4) meet the stability criteria that indicate the online computational burden is dramatically decreased. Then, the cost function is optimized among these possible alternatives to select the best control input. As a result, the state 2 is chosen as the best control input at this moment. Consequently, the computation required of the proposed method is limited concerning 27 switching configurations of the 3L-NPC inverter. Indeed, the number of loop interactions of the optimization problem for the standard FCS-MPC is 164 in contrast with the proposed method of 116. The detail improvement of the computational cost of the proposed approach with respect to traditional FCS-MPC is exhibited in Table 3. It is interesting to remark that, we have a different selection based on Lyapunov candidate function $\dot{V}$ and $\Delta V = V(k+1) - V(k)$ because of a discrete set control voltage. Mentioning in Fig. 6(d), at instant $t = 0.1632$ s, there are three switching states (state 2, 3 and 4) which have $\dot{V} < 0$. On the other hand, only state 1 has $\Delta V < 0$ as shown in Fig. 7. Hence, the derivative of the Lyapunov function $\dot{V}$ is better than its approximation ΔV to choose the switching decreasing Lyapunov function. This leads to the following formula:

$$u_{opt} = \arg\left\{ \min_{u_{k+1}\in\{-1,0,1\}^3} g\left(u_{k+1}\right) \right\}. \quad (28)$$
$$\text{subject to } \dot{V}(k+1) < 0$$

TABLE 3: Online computational load of two control strategies.

Interaction term	Standard FCS-MPC	Proposed approach
$\hat{i}_d(k+1),\ \hat{i}_q(k+1)$	1	1
$i_d^*(k),\ i_q^*(k)$	1	1
$u^p_{xZ-real}(k+1),\ i^p_{zx}(k+1)$	27	27
$\dot{V}(k+1)$	0	27
$i_d^p(k+2),\ i_q^p(k+2)$	27	12
n_{sw}	27	12
$u_z^p(k+2)$	27	12
$P_g^p(k+2),\ Q_g^p(k+2)$	27	12
$g(u_{k+1})$	27	12
Total	164	116

Finally, the proposed predictive control strategy is illustrated in Algorithm 1.

Algorithm 1: Algorithm of the proposed Lyapunov model predictive power control

Input: $i_g(k)$, $u_z(k)$, U_{dc}, $P_g^*(k)$ and $Q_g^*(k)$
Output: Switching signals S_a, S_b, S_c
Predict the grid current $\hat{i}_d(k+1)$ and $\hat{i}_q(k+1)$ from (17)
Compute the reference of the grid current $i_d^*(k)$ and $i_q^*(k)$ from (22)
Initialize the optimal cost function g_{opt} and switching state x_{opt}
for $i = 1$ to 27 **do**
  Compute the predictions with dead-time compensation: $u^p_{xZ-real}(k+1)$ and $i^p_{zx}(k+1)$ using (12) and (13)
  Evaluate the derivative of Lyapunov candidate function: $\dot{V}(k+1)$ based on (26)
  if $\dot{V}(k+1) < 0$ **then**
    Predict the current: $i_d^p(k+2)$ and $i_q^p(k+2)$ based on (18)
    Estimate the values: n_{sw} from (16)
    Predict the neutral-point voltage $u_z^p(k+2)$ from (19)
    Calculate the power: $P_g^p(k+2)$ and $Q_g^p(k+2)$ based on (11)

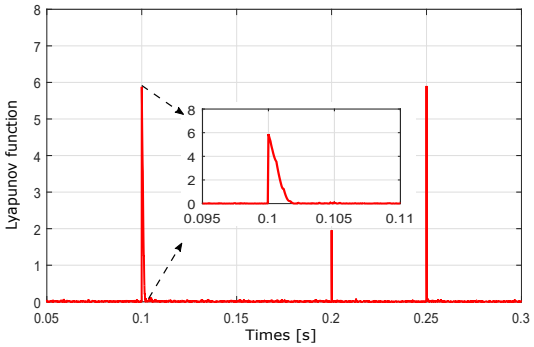

(a) Lyapunov function

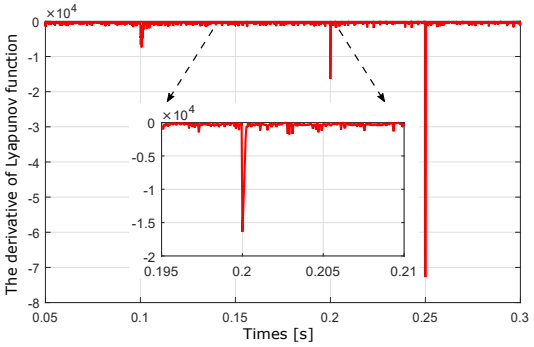

(b) The derivative of the Lyapunov function

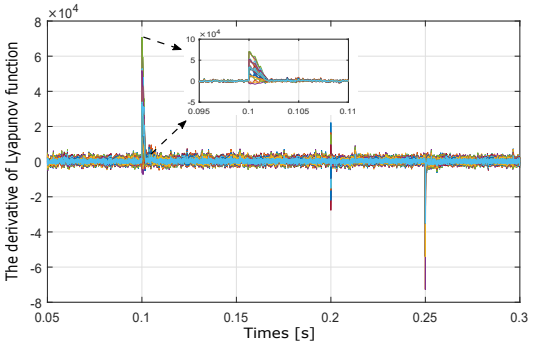

(c) The prediction derivative of Lyapunov function for all switching states

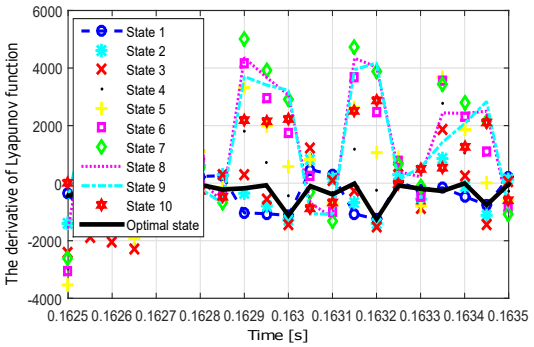

(d) The selection of the switching sequence relying on predicted stability and cost function minimization

FIGURE 6: The dynamic responses for the Lyapunov function and its derivative.

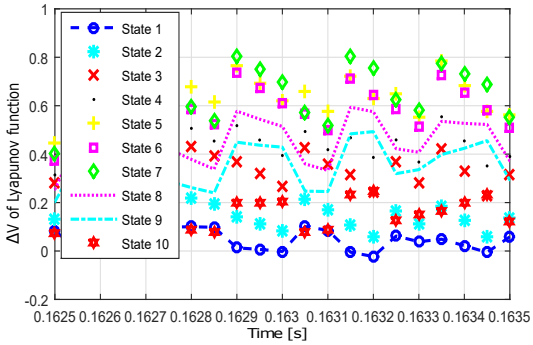

FIGURE 7: ΔV of Lyapunov function.

Calculate the cost function g from (28)
if $g < g_{opt}$ **then**
$g_{opt} = g;\ x_{opt} = i$
end if
end if
end for

IV. SIMULATION AND EXPERIMENTAL RESULTS

A. SIMULATION RESULTS

The control strategy is conducted within the Matlab/Simulink environment under different operating conditions to verify the feasibility of the proposed method. Table 4 shows the parameters of the controller and system.

TABLE 4: Parameters of the controller and system.

Parameters	Value	Representation
U_{dc}	600 [V]	DC-bus voltage
C	1000 [μF]	DC-bus capacitance
R_f	80 [$m\Omega$]	Filter resistance
L_f	10 [mH]	Filter inductance
T_s	50 [μs]	Sampling time
f_g	50 [Hz]	Grid frequency
U_g	380 [V]	Grid three-phase voltage
λ_{uz}	0.5	Weighting factor of voltage balance
λ_{sw}	0.01	Weighting factor of switching frequency reduction
K_d, K_q	1, 1	Positive gains of Lyapunov function
t_{on}, t_{off}	0.11, 0.24 [μs]	Turn-on/off time of IGBT
t_d	2 [μs]	Dead-time of IGBT

The mean absolute percentage error (MAPE) can be utilized to examine the control performance. Its expression is given by:

$$MAPE = \frac{1}{n}\sum_{k=1}^{n}\left|\frac{h_k^* - h_k}{h_k^*}\right|, \tag{29}$$

where h_k and h_k^* are the measurement and reference values, respectively.

On the other hand, the following expression proposed in [21] can be used to evaluate the average switching frequency (f_{sw}) of control method:

$$f_{sw} = \sum_{x=a,b,c}\frac{n_{sw_{1x}} + n_{sw_{2x}} + n_{sw_{3x}} + n_{sw_{4x}}}{12T_{sim}}, \tag{30}$$

where $n_{sw_{1x}}$, $n_{sw_{2x}}$, $n_{sw_{3x}}$ and $n_{sw_{4x}}$ represent the commutation of each inverter branch in the period (T_{sim}).

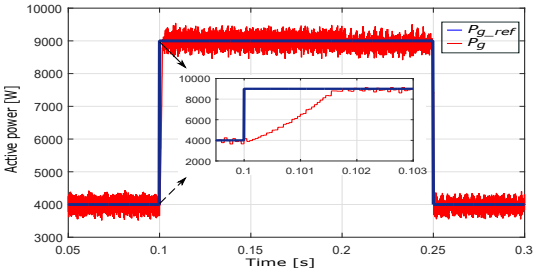

(a) Active power of the conventional MPC

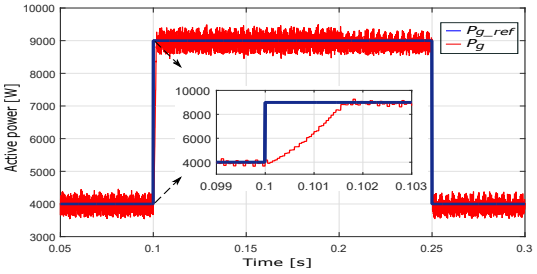

(b) Active power of the proposed method

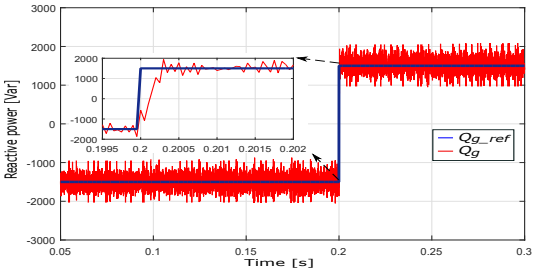

(c) Reactive power of the conventional MPC

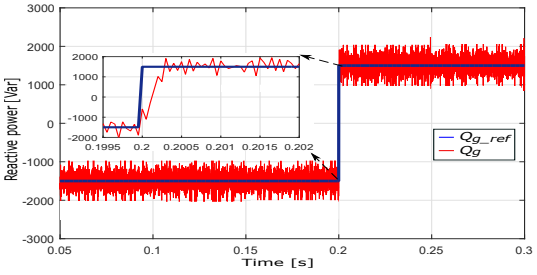

(d) Reactive power of the proposed method

FIGURE 8: The dynamic response of active and reactive powers for the conventional and proposed method.

In order to validate the control performance, a comparative study between the proposed method and the traditional FCS-MPC [21] is investigated under the different operating conditions and the same parameters. First we compare results considering no dead-time effect in the switches. To obtain the average frequency of switches $f_{sw} = 5$ kHz, the sampling time of the controllers is set at $T_s = 50$ μs. Various steps of the grid power are applied to demonstrate the validity of the proposed control scheme. The initial values of the active and reactive power references are 4 kW and -1.5 kVar, corresponding to the $PF = -0.94$. A step reference of active power (P_{g-ref}) from 4 kW to 9 kW is applied at time $t = 0.1$ s, then returned to 4 kW at $t = 0.25$ s. Fig. 8(b) shows the output active power and its reference of the proposed method. The reactive power demand is varied from -1.5 kVar to 1.5 kVar at $t = 0.2$ s relative to the leading power factor and lagging power factor, respectively as presented in Fig. 8(d). As highlighted in Fig. 8, the proposed method has the same control performance compared with the traditional FCS-MPC. Indeed, the active power of two controllers accomplishes steady-state of the dynamic response from 4 kW to 9 kW in about 1.5 ms. The MAPE of the active and reactive powers of the classical FCS-MPC are 3.33% and 12.17% while their corresponding values are 3.34% and 13.27% for the proposed method.

The steady-state performance of the grid current is performed with the THD for the traditional MPC of 1.96% (Fig. 9(b)) in comparison with the proposed method distortion of 2.0% (Fig. 9(d)). Fig. 9 illustrates the dynamic response and its Fast Fourier Transform (FFT) generated from Powergui toolbox, where the THD of the grid current satisfies the IEEE 519 standards. The obtained results indicate that the power ripples and THD of the grid current for the proposed method augment moderately compared to traditional MPC. This phenomenon is an expected trade-off to be accepted for including stability criteria of the closed-loop system in the design control of the FCS-MPC. Furthermore, the average computational time of the proposed technique is 19 μs in contrast to the conventional method of 29 μs in a 2.3 GHz, I5 5300 CPU. This means that we can increase the sampling frequency to improve control performance thanks to 34% reduction in computational burden. As a result, this control strategy underlines the importance of practical applications for the implementation with a low-cost processor. The quantitative comparisons of two controllers which comprehend the power ripples, THD of the current and computation time are summarized in Table 5.

TABLE 5: Comparison of control performance for two methods.

Performance	Method	
	Conventional FCS-MPC	Proposed method
MAPE of P_g	3.33%	3.34%
MAPE of Q_g	12.17%	13.27%
THD of i_{ag}	1.96%	2.0%
Minimum computation time	17 μs	8 μs
Maximum computation time	41 μs	30 μs
Average computation time	29 μs	19 μs

Moreover, the unbalance of the DC-bus capacitor voltage is also discussed in our research. As shown in Fig. 10, the capacitor voltages keep the balance with MAPE of neutral-point voltage for the conventional method of 0.18% and 0.17% for the proposed method, respectively.

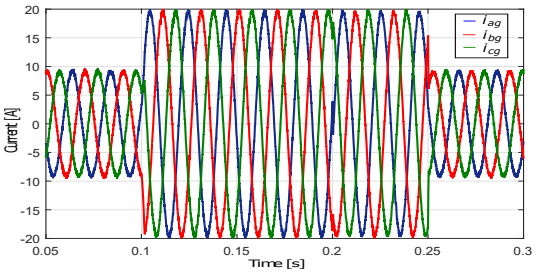

(a) Transient current response of the conventional method

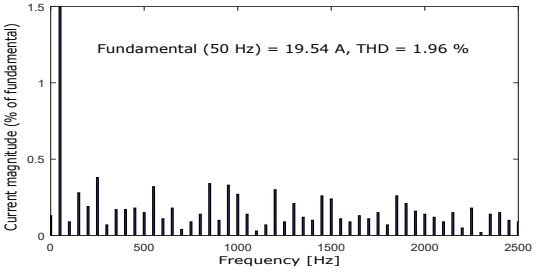

(b) Harmonic spectrum of the current for the conventional method

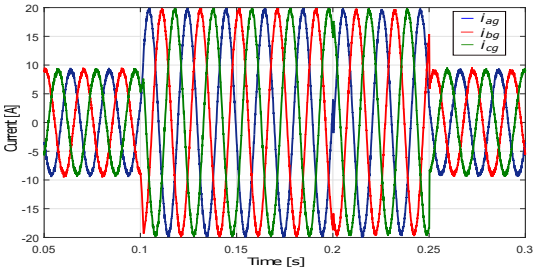

(c) Transient current response of the proposed method

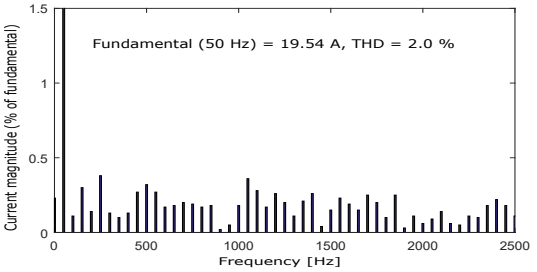

(d) Harmonic spectrum of the current for the proposed method

FIGURE 9: The transient response and harmonic spectrum of the grid current for the conventional method and proposed method without dead-time effect.

With the aim to confirm the suppression of dead-time influence, the harmonic spectrum of current obtained with dead-time effects for the uncompensated and compensated case is also investigated in our research. Fig. 11(a) indicates that the amplitude of the order harmonics for the uncompensated case is large due to the dead-time effect. In fact, comparing with the ideal case (Fig. 9(d)) the THD of the grid current for the uncompensated case is increased to 2.9% from 2.0%. On the other hand, the components of the harmonic spectrum are

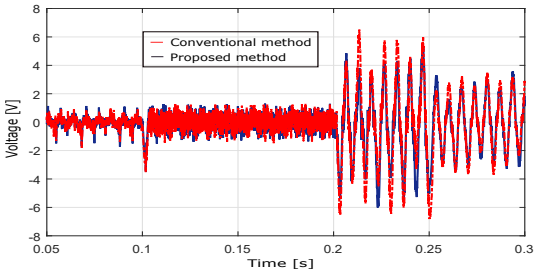

FIGURE 10: Neutral-point voltage response.

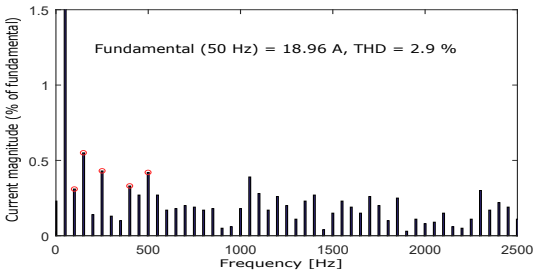

(a) FFT of the grid current without compensation

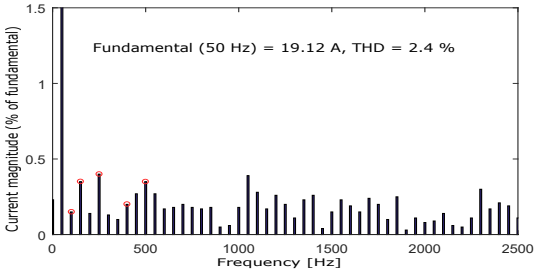

(b) FFT of the grid current with compensation

FIGURE 11: Grid current spectrum with and without dead-time compensation.

reduced, especially the 2nd, 3rd, 5th, 8th and 10th compared with not dead-time compensation as depicted in Fig. 11(b). In real system, the compensation can not completely eliminate this effect because of the influence of various ingredients such as propagation delay or device non-linearity. However, the findings of our research might help to have important implications for analyzing and solving the dead-time impact.

To validate the robustness of the proposed approach with parameter variations, a test with a reduction of 50% in the filter resistance and inductance is carried out in this study. In this case, the active power is changed from 4 kW to 9 kW at instant $t = 0.15$ s while the reactive power is kept to zero. As can be seen in Fig. 12, the proposed method is able to achieve sinusoidal grid current with the small ripple of the current and powers.

B. EXPERIMENTAL RESULTS

A scaled down prototype, depicted in Fig. 13, was built in the laboratory to confirm the proficiency of the proposed control scheme. A DSP of TMS320F28335 was

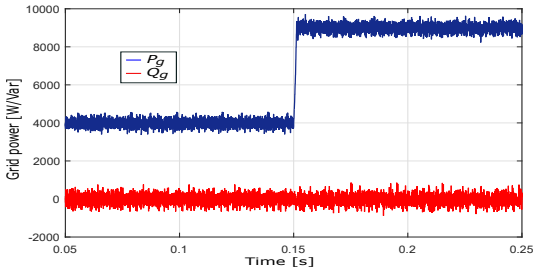

(a) Grid power response

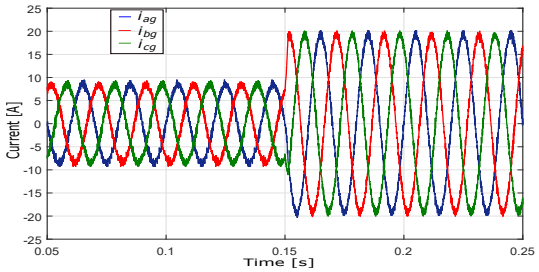

(b) Grid current response

FIGURE 12: Grid power and current responses with parameter variations.

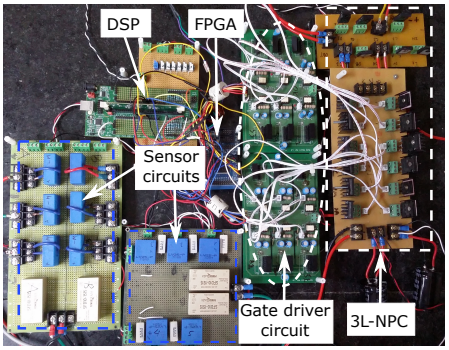

FIGURE 13: Experimental laboratory prototype.

utilized to apply the control technique. The S-function builder block with embedded coder was used to program the proposed algorithm. The 3L-NPC inverter consists of six clamping diodes FFPF10UA60ST and twelves modules IGBT NGTB10N60FG. Furthermore, two capacitors LGG2G102MELC50 1000 mF-400 V were applied for DC-bus voltage. The filter value and dead-time of the switches are similar to the simulation parameters. The LV 25-P and LA 25-P transducers were employed to measure the capacitor voltages, grid voltage, and current.

The DC-bus voltage is kept at 600 V. The line-to-line grid voltage is fixed to 220 V and 60 Hz of frequency. The sampling time greatly influences the control performance of the FCS-MPC scheme. Small sampling time will result in high performance of the system but require a fast control processor to ensure a large number of calculations necessary. This leads to an increase in the cost of the system, causing a challenge in industrial applications. On the other hand, the quality of the system is deteriorated with a large sampling period. For this reason, the sampling time is set to 100μs which is suitable for a clock frequency of TMS320F28335 (150 Mhz) and enhances the benefit of the low computational burden of the proposed method. The steady-state and transient behavior are investigated under the change in the active and reactive powers to validate the capability of the control strategy. In the first test, the active power (P_g) and reactive powers (Q_g) are set to 2 kW and 0 Var, respectively. The experimental results of grid power and current in steady-state are demonstrated in Fig. 14. These results prove that the grid power exchanges of the proposed technique are kept constant and closed to their references. As illustrated in Fig. 14(b), the grid current is approximately a sinusoidal waveform due to the imperfect sine wave of grid voltage. Moreover, the proposed control strategy is also investigated in the lagging power factor condition. In this case, the reference of active and reactive powers was set to 2000 W and 1000 Var, respectively. Fig. 15 indicates that the proposed method achieved a proper power tracking ability under the change in the power factor value.

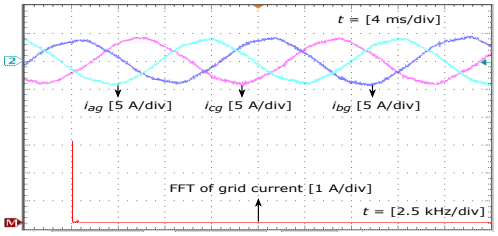

(a) Three-phase grid current

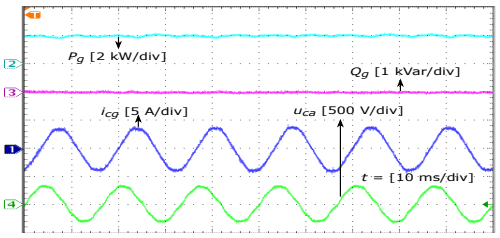

(b) Grid power, voltage and current

FIGURE 14: Steady-state results of the proposed method under the condition $P_g = 2000$ W and $Q_g = 0$ Var.

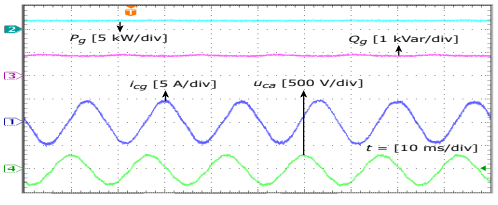

FIGURE 15: Steady-state results of the proposed method under the condition $P_g = 2000$ W and $Q_g = 1000$ Var.

In the second test, a comparison with the conventional FCS-MPC is carried out with a step transition in grid active power from 0 to 2 kW to verify the capability of power

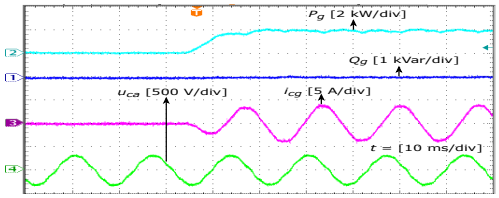

(a) Grid power and current responses of the conventional method

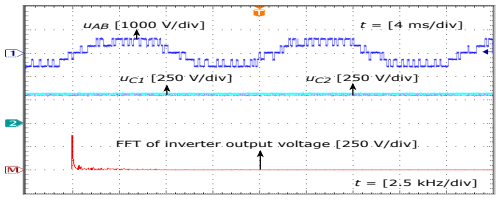

(b) Inverter and capacitor voltages of the conventional method

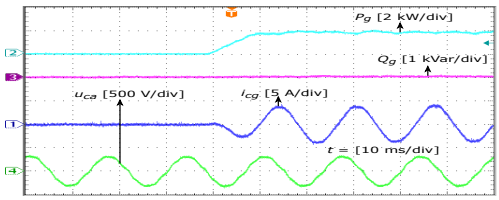

(c) Grid power and current responses of the proposed method

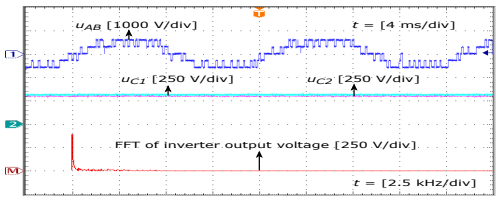

(d) Inverter and capacitor voltages of the proposed method

FIGURE 16: Transient responses under the step change of active power from 0 to 2 kW.

tracking. The reactive power is kept to zero, corresponding to the unity power factor. As shown in Fig. 16, two methods have the same control performance. In fact, the active power and grid current track the new reference values after a short transient time. The reactive power is maintained null despite of this transient response. Moreover, the balance of the DC-link capacitor voltages is assured even though the sudden change in active power as shown in Fig. 16(d). As can be seen in Fig. 16(c), the proposed technique guarantees a satisfying decoupling of active and reactive power control.

A Fluke 43B instrument is used to measure the THD of the grid current. As demonstrated in Fig. 17, the THD of the grid current for the conventional method without compensation is higher than its value of the proposed method. We argue that this value is due to the important dead-time, causing a deterioration of the quality of the current. Consequently, we believe that our method can be useful in compensation of dead-time effect for the power converters. The comparison of the

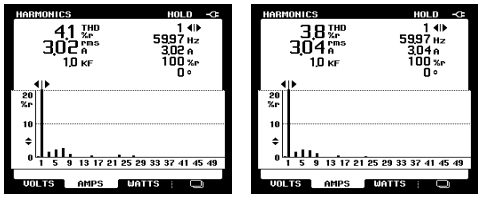

(a) Conventional method (b) Proposed method

FIGURE 17: THD results of grid current for two control methods.

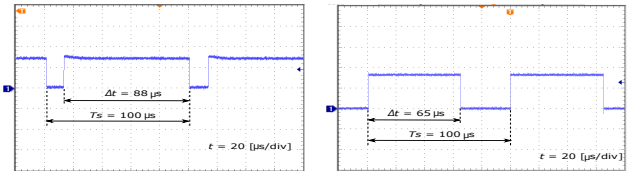

(a) Conventional method (b) Proposed method

FIGURE 18: Execution time of two controllers.

execution time between the conventional and the proposed method is demonstrated in Fig. 18. Based on these experiments the proposed algorithm reduces 26% of execution time required from 88 μs to 65 μs compared to the conventional method. Therefore, our research provides a novel solution for addressing the problem due to the computational burden and dead-time effect. This benefit can apply to the low-cost processor, leading to a reduction in the cost of the system.

V. CONCLUSION

This paper described the advantages of a power control scheme based on model predictive control for a grid-tie 3L-NPC inverter. A Lyapunov function is employed in the control design to guarantee the stability of the closed-loop system and decrease the computational burden required compared to the traditional FCS-MPC method. Moreover, the dead-time compensation is implemented directly into the controller while maintaining a satisfactory power tracking ability. A comparative study indicates that the proposed method obtains competitive control performance in terms of power and lower THD of the current in comparison with the conventional approach. Simulation and laboratory results have proved the feasibility of this advanced control strategy.

REFERENCES

[1] R. C. Portillo et al.,"Modeling Strategy for Back-to-Back Three-Level Converters Applied to High-Power Wind Turbines," IEEE Transactions on Industrial Electronics, vol. 53, no. 5, pp. 1483–1491, Oct 2006.

[2] M. Schweizer, T. Friedli, and J. W. Kolar,"Comparative Evaluation of Advanced Three-Phase Three-Level Inverter/Converter Topologies Against Two-Level Systems," IEEE Transactions on Industrial Electronics, vol. 60, no. 12, pp. 5515–5527, Dec 2013.

[3] U. Choi, J. Lee, and K. Lee,"New Modulation Strategy to Balance the Neutral-Point Voltage for Three-Level Neutral-Clamped Inverter Systems," IEEE Transactions on Energy Conversion, vol. 29, no. 1, pp. 91–100, March 2014.

[4] C. Xiang, C. Shu, D. Han, B. Mao, X. Wu, and T. Yu,"Improved Virtual Space Vector Modulation for Three-Level Neutral-Point-Clamped Converter With Feedback of Neutral-Point Voltage," IEEE Transactions on Power Electronics, vol. 33, no. 6, pp. 5452–5464, June 2018.
[5] V. Q. B. Ngo, M. K. Nguyen, T. T. Tran, Y. C. Lim, and J. H. Choi,"A Simplified Model Predictive Control for T-Type Inverter with Output LC Filter," Energies, vol. 12, no. 1, 2019.
[6] H. T. Do, T. D. Dang, H. V. A. Truong, and K. K. Ahn,"Maximum Power Point Tracking and Output Power Control on Pressure Coupling Wind Energy Conversion System," IEEE Transactions on Industrial Electronics, vol. 65, no. 2, pp. 1316–1324, Feb 2018.
[7] H. R. Teymour, D. Sutanto, K. M. Muttaqi, and P. Ciufo,"Solar PV and Battery Storage Integration using a New Configuration of a Three-Level NPC Inverter With Advanced Control Strategy," IEEE Transactions on Energy Conversion, vol. 29, no. 2, pp. 354–365, June 2014.
[8] B. M. Wilamowski and J. D. Irwin, Power Electronics and Motor Drives. CRC Press, 2017.
[9] M. Malinowski, M. P. Kazmierkowski, S. Hansen, F. Blaabjerg, and G. D. Marques,"Virtual-flux-based direct power control of three-phase PWM rectifiers," IEEE Transactions on Industry Applications, vol. 37, no. 4, pp. 1019–1027, July 2001.
[10] M. Castilla, J. Miret, A. Camacho, J. Matas, and L. G. de Vicuna,"Reduction of Current Harmonic Distortion in Three-Phase Grid-Connected Photovoltaic Inverters via Resonant Current Control," IEEE Transactions on Industrial Electronics, vol. 60, no. 4, pp. 1464–1472, April 2013.
[11] A. Bouafia, F. Krim, and J. Gaubert,"Fuzzy-Logic-Based Switching State Selection for Direct Power Control of Three-Phase PWM Rectifier," IEEE Transactions on Industrial Electronics, vol. 56, no. 6, pp. 1984–1992, June 2009.
[12] F. Sebaaly, H. Vahedi, H. Y. Kanaan, N. Moubayed, and K. Al-Haddad,"Design and Implementation of Space Vector Modulation-Based Sliding Mode Control for Grid-Connected 3L-NPC Inverter," IEEE Transactions on Industrial Electronics, vol. 63, no. 12, pp. 7854–7863, Dec 2016.
[13] V. Q. B. Ngo, P. Rodriguez-Ayerbe, and S. Olaru,"Model predictive control with two-step horizon for three-level neutral-point clamped inverter," in Proc. 20th International Conference on Process Control, June 2015, pp. 585–590.
[14] H. Moon, J. Lee, and K. Lee,"A Robust Deadbeat Finite Set Model Predictive Current Control Based on Discrete Space Vector Modulation for a Grid-Connected Voltage Source Inverter," IEEE Transactions on Energy Conversion, vol. 33, no. 4, pp. 1719–1728, Dec 2018.
[15] G. A. Papafotiou, G. D. Demetriades, and V. G. Agelidis,"Technology Readiness Assessment of Model Predictive Control in Medium and High-Voltage Power Electronics," IEEE Transactions on Industrial Electronics, vol. 63, no. 9, pp. 5807–5815, Sept 2016.
[16] Y. Yang, H. Wen, and D. Li,"A Fast and Fixed Switching Frequency Model Predictive Control With Delay Compensation for Three-Phase Inverters," IEEE Access, vol. 5, pp. 17904–17913, 2017.
[17] S. Kouro, M. A. Perez, J. Rodriguez, A. M. Llor, and H. A. Young,"Model Predictive Control: MPC's Role in the Evolution of Power Electronics," IEEE Industrial Electronics Magazine, vol. 9, no. 4, pp. 8–21, Dec 2015.
[18] V. Q. B. Ngo, P. Rodriguez-Ayerbe, S. Olaru, and S. Niculescu,"Model predictive power control based on virtual flux for grid connected three-level neutral-point clamped inverter," in Proc. 18th European Conference on Power Electronics and Applications, Sept 2016, pp. 1–10.
[19] A. Imura, T. Takahashi, M. Fujitsuna, T. Zanma, and S. Doki,"Dead-time compensation in model predictive instantaneous-current control," in Proc. 38th Annual Conference on IEEE Industrial Electronics Society, Oct 2012, pp. 5037–5042.
[20] A. Kuznietsov, S. Wolf, and T. Happek,"Model predictive control of a voltage source inverter with compensation of deadtime effects," in Proc. IEEE International Conference on Industrial Technology, March 2015, pp. 2532–2536.
[21] J. Rodriguez and P. Cortes, Predictive Control of Power Converters and Electrical Drives. John Wiley, 2012.
[22] X. Liu, D. Wang, and Z. Peng,"Cascade-Free Fuzzy Finite-Control-Set Model Predictive Control for Nested Neutral Point-Clamped Converters With Low Switching Frequency," IEEE Transactions on Control Systems Technology, vol. 27, no. 5, pp. 2237-2244, Sept 2019.
[23] Y. Yang, S. Tan, and S. Y. R. Hui,"Adaptive Reference Model Predictive Control With Improved Performance for Voltage-Source Inverters," IEEE Transactions on Control Systems Technology, vol. 26, no. 2, pp. 724–731, March 2018.
[24] S. Vazquez, J. Rodriguez, M. Rivera, L. G. Franquelo, and M. Norambuena,"Model Predictive Control for Power Converters and Drives: Advances and Trends," IEEE Transactions on Industrial Electronics, vol. 64, no. 2, pp. 935–947, Feb 2017.
[25] W. Wu and D. Wang,"An Optimal Voltage-Level Based Model Predictive Control Approach for Four-Level T-Type Nested Neutral Point Clamped Converter With Reduced Calculation Burden," IEEE Access, vol. 7, pp. 87458–87468, 2019.
[26] M. H. Nguyen and S. Kwak,"Simplified Indirect Model Predictive Control Method for a Modular Multilevel Converter," IEEE Access, vol. 6, pp. 62405–62418, 2018.
[27] I. S. Mohamed, S. Rovetta, T. D. Do, T. Dragicevic, and A. Diab,"A Neural-Network-Based Model Predictive Control of Three-Phase Inverter With an Output LC Filter," IEEE Access, pp. 1-1, 2019.
[28] C. Xia, T. Liu, T. Shi, and Z. Song,"A Simplified Finite-Control-Set Model-Predictive Control for Power Converters," IEEE Transactions on Industrial Informatics, vol. 10, no. 2, pp. 991–1002, May 2014.
[29] S. Vazquez et al.,"Model Predictive Control for Single-Phase NPC Converters Based on Optimal Switching Sequences," IEEE Transactions on Industrial Electronics, vol. 63, no. 12, pp. 7533–7541, Dec 2016.
[30] R. P. Aguilera and D. E. Quevedo,"Predictive Control of Power Converters: Designs With Guaranteed Performance," IEEE Transactions on Industrial Informatics, vol. 11, no. 1, pp. 53–63, Feb 2015.
[31] R. P. Aguilera and D. E. Quevedo,"On stability and performance of finite control set MPC for power converters," in Workshop on Predictive Control of Electrical Drives and Power Electronics, 2011, pp. 55-62.
[32] M. P. Akter, S. Mekhilef, N. M. L. Tan, and H. Akagi,"Modified Model Predictive Control of a Bidirectional AC–DC Converter Based on Lyapunov Function for Energy Storage Systems," IEEE Transactions on Industrial Electronics, vol. 63, no. 2, pp. 704–715, Feb 2016.
[33] S. Kwak, S. Yoo and J. Park,"Finite control set predictive control based on Lyapunov function for three-phase voltage source inverters," IET Power Electronics, vol. 63, no. 2, pp. 2726-2732, 2014.
[34] V. Q. B. Ngo, P. Rodriguez-Ayerb, S. Olaru, and S.-I. Niculescu,"Model Predictive Direct Power Control of Doubly Fed Induction Generator with Dead-Time Compensation," IFAC PapersOnLine, vol. 7, no. 11, pp. 8752–8757, 2017.
[35] M. Sprenger, T. Barth, R. Alvarez, M. Tannhaeuser, and S. Bernet,"Experimental verification of direct dead-time Control and DC-link neutral-point balancing of a three level neutral-point-clamped (3L-NPC) VSC," in Proc. IEEE Energy Conversion Congress and Exposition, Sept 2013, pp. 409–413.
[36] J. Rodriguez et al.,"State of the Art of Finite Control Set Model Predictive Control in Power Electronics," IEEE Transactions on Industrial Informatics, vol. 9, no. 2, pp. 1003–1016, May 2013.
[37] G. Prior and M. Krstic,"Quantized-Input Control Lyapunov Approach for Permanent Magnet Synchronous Motor Drives," IEEE Transactions on Control Systems Technology, vol. 21, no. 5, pp. 1784–1794, Sept 2013.

VAN-QUANG-BINH NGO received the M.Sc. degree in 2009 from the Da Nang University of Science and Technology, Vietnam and, the Ph.D. degree in 2017 from CentraleSupélec-Paris Saclay University, France, all in automation. He was appointed a lecturer at the Hue University of Education, Vietnam in 2004 and promoted to assistant professor in 2017. He was a Postdoctoral Researcher at the Department of Electrical Engineering, Chonnam National University, South Korea in 2018. His research interests include multilevel converters topology, predictive control for power converters and electrical drives and their applications in renewable energy systems.

HIEP-VU VAN received the B.E. degree in electronics and telecommunications engineering from Ton Duc Thang University, Vietnam, in 2005, the degree in business administration from the University of Economy, Ho Chi Minh City, Vietnam, in 2007, and the Ph.D. degree in electrical engineering from the University of Ulsan, South Korea, in 2013. He is currently a Research Fellow with the University of Ulsan. His current research interests include cognitive radio and next-generation wireless communication systems.

VIET-TUAN PHAM received the B.E. degree (2005), M.E. degree (2011) in Electronics and Telecommunications Engineering from Ho Chi Minh City University of Technology, Vietnam, and Ph.D degree (2018) in Electrical and Computer Engineering from University of Ulsan, South Korea. He was as Postdoctoral Researcher at the Multimedia Communications System Laboratory, University of Ulsan, South Korea (2019). His research interests include optimizations, SWIPT systems, and machine learning.

HUU-NHAN NGUYEN (S'14-M'19) received the B.S. degree in electrical engineering from Ho Chi Minh City University of Technology, Vietnam, in 2010, and the Ph.D. degree in electrical engineering from the University of Ulsan, Korea, in 2017. He is currently with the Institute of Research and Development (IRD), Duy Tan University, Da Nang, Vietnam, where he is engaged in teaching and research in the areas of automatic control and power electronics. His research interests include power conversion, advanced controls, and electrical machine drives.

PEDRO RODRIGUEZ-AYERBE received the technical engineering Diploma in electronics from Mondragon University, Arrasate, Spain, in 1993, and the Engineering degree in Electrical Engineering from SUPELEC, Gif sur Yvette, France, in 1996. In 2003, he received the Ph.D. degree in Automatic Control from SUPELEC and the Université Paris Sud, Orsay, France. He is currently a Professor in CentraleSupélec, member of the CNRS Laboratory of Signals and Systems being part of the Paris-Saclay University in France. His research interests include constrained predictive control and robust control theory.

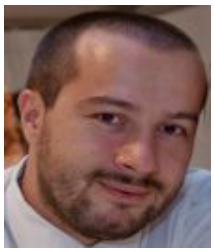

SORIN OLARU is a Professor in CentraleSupélec, member of the CNRS Laboratory of Signals and Systems and of the INRIA team DISCO, all these institutions being part of the Paris-Saclay University in France. His research interests are encompassing the optimization-based control design, set-theoretic characterization of constrained dynamical systems as well as the numerical methods in control. He is currently involved in research projects related to embedded predictive control, fault tolerant control and time-delay systems.

HOANG-THINH DO received the B.S. degree from Hochiminh City University of Technology in Mechanical Engineering, Vietnam in 2010, the M. Sc. degree in from University of Ulsan, Korea in 2013 and the Ph.D. degree with the title "A Study on Hemispherical-float Wave Energy Converter Using Hydraulic Transmission - Proposition, Modeling and Experiment" from University of Ulsan, Korea in 2016. He is currently a Researcher and Lecturer in the Division of Computational Mechatronics, Institute for Computational Science, Ton Duc Thang University, Hochiminh City, Vietnam. His research interests focus on Mechatronics, Hydraulic Systems and Renewable Energy.